Plasma Parameters from Quasi-Thermal Noise Observed by Parker Solar Probe: A New Model for the Antenna Response

Mihailo M. Martinović[1,2], Antonije R. Đorđević[3,4], Kristopher G. Klein[1], Milan Maksimović[2], Karine Issautier[2], Mingzhe Liu[2], Marc Pulupa[5], Stuart D. Bale[5,6,7,8], Jasper S. Halekas[9]and Michael D. McManus[5]

[1]Lunar and Planetary Laboratory, University of Arizona, Tucson, AZ 85721, USA.
[2]LESIA, Observatoire de Paris, Université PSL, CNRS, Sorbonne Université, Université de Paris, 92195 Meudon, France.
[3]School of Electrical Engineering, University of Belgrade, 11000 Belgrade, Serbia
[4]Serbian Academy of Sciences and Arts, 11000 Belgrade, Serbia
[5]Space Sciences Laboratory, University of California, Berkeley, CA 94720-7450, USA
[6]School of Physics and Astronomy, Queen Mary University of London, London E1 4NS, UK
[7]Physics Department, University of California, Berkeley, CA 94720-7300, USA
[8]The Blackett Laboratory, Imperial College London, London, SW7 2AZ, UK
[9]Department of Physics and Astronomy, University of Iowa, IA 52242, USA

Key Points:

- We model the antenna response for the unique geometry of linear dipole antenna containing a gap between arms
- This antenna response is used to improve plasma parameters determination from the observed quasi-thermal noise spectrum
- The proposed model yields derived electron parameters consistent with those from the SWEAP/SPAN instrument suite onboard Parker Solar Probe

Corresponding author: Mihailo M. Martinović, `mmartinovic@arizona.edu`

Abstract

Quasi-Thermal Noise (QTN) spectroscopy is a reliable diagnostic routinely used for measuring electron density and temperature in space plasmas. The observed spectrum depends on both antenna geometry and plasma kinetic properties. Parker Solar Probe (PSP), launched in 2018, is equipped with an antenna system consisting of two linear dipoles with a significant gap between the antenna arms. Such a configuration, not utilized on previous missions, cannot be completely described by current models of the antenna response function. In this work, we calculate the current distribution and the corresponding response function for the PSP antenna geometry, and use these results to generate synthetic QTN spectra. Applying this model to the Encounter 7 observations from PSP provides accurate estimations of electron density and temperature, which are in very good agreement with particle analyzer measurements.

Plain Language Summary

Parker Solar Probe (PSP) is a NASA mission that is travelling much closer to the Sun than any previous spacecraft. A primary consequence of this specific trajectory are multiple adaptations in the design of instruments (radio instruments, magnetometers, particle detectors etc.) and their complex accommodations on the spacecraft. This article investigates effects of the specific PSP radio antenna geometry to high-frequency electric field observations. We apply Quasi-Thermal Noise Spectroscopy, a well established method for determining plasma density and temperature, to PSP instruments, and validate the results by comparing the parameter values from radio observations to the ones obtained by particle analyzers onboard PSP.

1 Introduction

QTN spectroscopy, theoretically described more than half a century ago (Andronov, 1966; Fejer & Kan, 1969), is a powerful tool to diagnose space plasmas using a passive electric antenna related to a sensitive radio receiver. Since this method was fully expanded to solar wind and pioneered aboard *ISEE-3* (Meyer-Vernet, 1979; Hoang et al., 1980), it has been routinely used to infer in-situ electron densities and temperatures on various missions in the solar wind: *IMP-6* (Kellogg, 1981), *Ulysses* (Maksimovic et al., 1995; Issautier et al., 1996, 1999; Le Chat et al., 2011), *Wind* (Maksimovic et al., 1998; Issautier et al., 2005; Martinović et al., 2020), *STEREO* (Zouganelis et al., 2010; Martinović et al., 2016), and planetary missions such as *Cassini* (Moncuquet et al., 1997, 2005).

QTN spectrum depends on two sets of inputs: 1) kinetic plasma properties, reflected through the electron VDF shape, and described by characteristic plasma functions that depend on the VDF, and 2) antenna shape and configuration, described by the antenna response function (ARF). For a comprehensive review of the QTN spectroscopy theory see e.g. Meyer-Vernet and Perche (1989); Meyer-Vernet et al. (2017). All the aforementioned missions have significantly different characteristic spectra due to different antenna configurations. These differences can be summed up in two broad categories: 1) the visibility of the plasma peak just above the electron plasma frequency $f_p = \omega_p/2\pi = (2\pi)^{-1}\sqrt{n_e e^2/\epsilon_0 m_e}$, depending on the ratio between the antenna length L_{ant} and Debye length L_D, where $L_D = \sqrt{\epsilon_0 k_b T_e/n_e e^2}$ and 2) the effects of the impact noise, determined by the ratio of the antenna length to its radius L_{ant}/a_{ant}. Here, ϵ_0 is the dielectric permittivity of vacuum, k_b is the Boltzmann constant, and n_e, e and m_e are electron density, charge and mass, respectively. A common feature of spacecraft launched before *PSP* was a dipole antenna configuration with a negligibly small gap between the antenna arms, and the spacecraft body effects being also considered as negligible. The *PSP* FIELDS suite (Bale et al., 2016) is equipped with a set of two wire dipoles, with each arm $L_{ant} = 2$m long. The spacecraft (SC) body separates the antenna ports, creating a gap between the arms of each dipole of $2d = 2.98$m, a length comparable to L_{ant}. Configurations that fea-

ture the gap operate only on *PSP* FIELDS (Bale et al., 2016) and *Solar Orbiter* Radio and Plasma Waves (RPW) (Maksimović, Bale, Chust, et al., 2020) instruments, and initial observations showed that the total electron density could be inferred by locating the peak of the signal at $f_p \sim \sqrt{n_e}$ (Bale et al., 2019). However, the shape of the observed QTN spectra cannot be modelled by the ARFs derived for the case of dipoles without a gap (Kuehl, 1966, 1967). As the discrepancies due to this gap primarily appear in the vicinity of the plasma peak, preliminary studies were able to estimate electron core temperature T_c (Moncuquet et al., 2020) and total temperature T_e (Maksimović, Bale, Berčič, et al., 2020; Liu et al., 2021) by separately analyzing power levels below and above f_p, respectively.

The primary task of this paper is to characterize the FIELDS QTN spectrum shape given the unique instrument configuration by providing a single model valid both below and above f_p. To accomplish this, in Section 2 we derive the ARF using the antenna and (SC) current distribution calculated using the AWAS software (Đorđević et al., 2002). Then, in Section 3 we calculate the theoretical model of the QTN spectrum and fit it to observations from *PSP* Encounter 7 (E7) for periods where the antenna was unbiased. The results show very good agreement with observations obtained by the SWEAP SPAN instrument suite (Kasper et al., 2016; Whittlesey et al., 2020) and previous preliminary QTN spectrum processing (Moncuquet et al., 2020). Finally, we discuss the future use of this model, as well as potential shortcomings in Section 4.

2 Methods

2.1 FIELDS instrument observations

On *PSP*, the RFS component of the FIELDS suite collects the electric field fluctuations up to 19.2 MHz (Pulupa et al., 2017). Within RFS, LFR and HFR cover frequency ranges of 10 kHz – 1.7 MHz and 1.3 – 19.2 MHz, respectively, both with 64 logarithmically spaced frequencies, providing $\sim 4.5\%$ resolution. The measurements of interest for this work are collected in dipole mode, where the difference of voltages at the antenna terminals is processed using a Polyphase Filter Bank and Fast Fourier Transform algorithm. The spectra downloaded to ground at standard $\sim 3.5s$ cadence are averages of several tens of sampled spectra, where the statistical uncertainty of the power in each averaged spectrum is held below 0.3 dB (Pulupa et al., 2017). During specified parts of each encounter, bias current is applied to the antennas in order to keep the antenna potential close to the potential of the undisturbed plasma. Applying the bias current maximizes the response of the low frequency voltage measurement to the electric field signals of interest, while minimizing the response to plasma density fluctuations. Unfortunately, the biased current produces an increased impact noise signal just below the plasma frequency. As compensating for this bias-induced signal is beyond the intended scope of this work, we will only focus on time periods where the FIELDS antennas were not biased. This approach was enabled during *PSP* E7, as unbiased intervals appear daily (Jan 15-22, 2021), lasting 2 times 4 minutes for each dipole. In this work, we focus on V1-V2 dipole, that operated with no bias during 05:48 - 05:52 and 17:48 - 17:52 each day. In lieu of applying an algorithm that filters out low-frequency non-QTN signal components, such as wave activity and instrument gain effects, from the spectrum (Martinović et al., 2020), we use only the signal above 100 kHz, corresponding to approximately $0.25 f_p$, avoiding the resistively coupled antenna regime (Bonnell et al., 2019). We derive the plasma parameters from both the full resolution observations, and one minute median values, with medians having a purpose of removing any short term signal pollution. Electron VDF moments—core and halo density and temperature, are found via standard Levenberg-Marquardt least square fit of merged LFR/HFR data and theoretical spectra explained below. Proton parameters are used as errorless initial input, and are provided by fitting the SPAN-i measured proton VDFs (see, e.g. Verniero et al. (2020)).

2.2 Quasi-Thermal Noise Spectroscopy

The QTN is modelled for a proton-electron plasma, with the electron VDF consisting of two isotropic Maxwellians—a thermal core and suprathermal halo, and the proton VDF being a charge-neutralizing background isotropic Maxwellian. The synthetic QTN spectrum $V^2(f)$ is calculated using contributions from electrons $V^2_{\rm qtn}$, protons $V^2_{\rm pn}$, impact (shot) noise $V^2_{\rm sn}$ and galaxy radiation $V^2_{\rm gal}$ as

$$V^2 = \Gamma^2\big(V^2_{\rm qtn} + V^2_{\rm pn} + V^2_{\rm sn} + V^2_{\rm gal}\big) + V^2_{\rm lfr}. \tag{1}$$

Here, Γ is the antenna gain and the instrument noise is estimated to be $V^2_{\rm lfr} \approx 2.3{\cdot}10^{-17}{\rm V}^2/{\rm Hz}$ (Bale et al., 2016; Maksimović, Bale, Berčič, et al., 2020). Proton noise $V^2_{\rm pn}$, important below f_p, is estimated assuming the solar wind velocity $\mathbf{v_{sw}}$ is perpendicular to the FIELDS antenna, using the functional form given by Equation 22 from Issautier et al. (1999). We find proton contribution to be small compared to the impact noise at low frequencies close to perihelion, in agreement with theoretical predictions (Meyer-Vernet et al., 2017), but it still must be included for analysis close to f_p. Impact noise $V^2_{\rm sn}$ is calculated using Equation 15 from Martinović et al. (2016), and is very small compared to $V^2_{\rm qtn}$ near the peak. The level of the galaxy radiation power $V^2_{\rm gal}$ is calculated using the model given by Novaco and Brown (1978), with same parameters used in the Encounter 1 (E1) study by Maksimović, Bale, Berčič, et al. (2020). The galaxy and instrument noise signals are non-negligible only at very high frequency end of the spectrum and are expected to have only a minor contribution to the estimated values of halo temperature. For an isotropic Maxwellian, the electron contribution is (Chateau & Meyer-Vernet, 1989)

$$V^2_{\rm qtn}(\omega) = \frac{16 m_e \omega_p^2}{\pi \epsilon_0} \int_0^\infty \frac{B(k,\omega)F(k)}{k^2 |\epsilon_L(k,\omega)|^2}\, dk. \tag{2}$$

Plasma VDF functions $B(k,\omega)$ and $\epsilon_L(k,\omega)$ describe total amount of energy of the plasma and its response to fluctuations, respectively. These two functions are determined by plasma properties only, are not affected by the instrumentation and are explained in detail elsewhere (Meyer-Vernet & Perche, 1989; Martinović, 2016). The ARF $F(\mathbf{k})$ is given as a Fourier transform of the antenna current $\mathbf{j_a}(\mathbf{k})$ along the dipole, normalized to a value at the antenna terminals I_a, and integrated over the entire solid angle Ω for a given value of wavevector $\mathbf{k}$

$$F(k) = \frac{1}{32\pi} \int \frac{|\mathbf{k}\cdot\mathbf{j_a}(\mathbf{k})|^2}{I_a^2} d\Omega \tag{3}$$

From Equation 3 it is clear that the structure of the antenna current distribution $\mathbf{j_a}(\mathbf{r})$ significantly impacts the determination of the ARF.

2.3 Determination of current distribution via AWAS software

In order to characterize the antenna current distribution, we use the AWAS software package (Đorđević et al., 2002). AWAS is a versatile program for analyzing wire antennas and scatterers assembled from arbitrarily located and interconnected straight-line segments. Wire antennas can be modeled in free space, as done below, or located above a perfectly conducting plane, and can be analyzed in transmitting or receiving modes to calculate port matrix parameters, current distribution, near fields, and far fields.

The *top panel* of Figure 1 shows the 2D AWAS model of *PSP*. The SC body (shaded in grey) is approximated by a simple set of four orthogonal conductive wires, marked as segments 1-4 (blue numbers), extending between the node (reference point in the coordinate system marked by a red number) 1 and 2-5, respectively. The two dipoles are modeled as pairs of segments (5,7) and (6,8). Ports (antenna terminals) are marked by green dots and modelled as ideal current generators. Dimensions of segments reflect the FIELDS configuration, with wire segments 1-4 that replace the SC body being 1.49 m long, and antenna segments 5-8 2 m long (Bale et al., 2016). We assign the x axis to a line of a

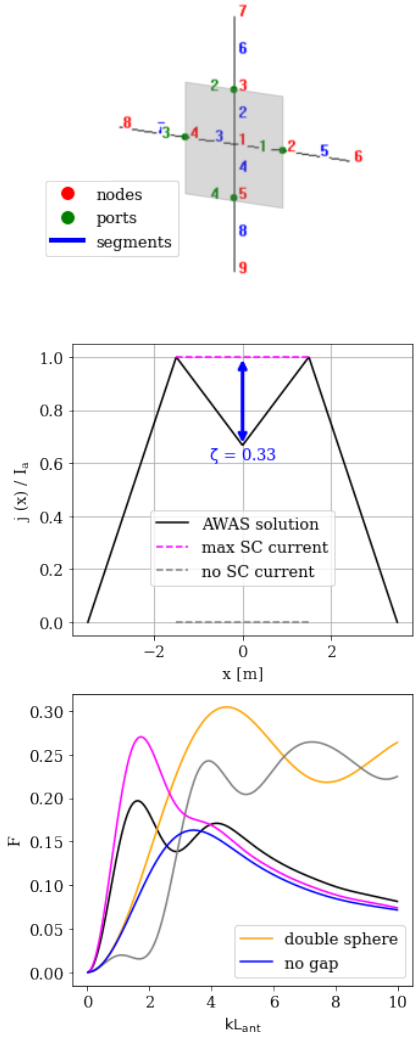

Figure 1. *Top: PSP* model in AWAS, with nodes (red), ports (green), and segments (blue) indicated (with labels for segment 1 and port 1 overlapped on each other). The SC body, which the model replaces with wires, is shaded in grey. *Middle:* AWAS solution for the current distribution between nodes 6 and 8 from the *top panel* (black), compared to models with the current flowing through the SC body having maximum (pink) (Meyer-Vernet & Perche, 1989) or zero value (grey). The current drops by a factor of $\zeta \approx 1/3$ compared to the values at antenna terminals. *Bottom:* Antenna response function calculated for various antenna configurations described in the text. The color coding for the unlabeled lines is the same as on the *middle panel*.

linear dipole extending between nodes 6 (x = 3.49 m) and 8 (x = -3.49 m), where the point of origin is at the center of the SC 2D quadratic geometry.

Once the antenna geometry is set, AWAS calculates currents and fields in and around antennas by solving a two-potential equation (see, e.g. (Đorđević et al., 1979; Popović et al., 1982)). This equation is numerically solved using the method of moments (Harrington, 1993) with the current distribution approximated by a polynomial (Đorđević et al., 1991). This way, we provide values of the antenna current at any point within segments 1-8. Details of the procedure are given in Chapter 6 of (Đorđević et al., 2002).

We model the system as a transmitting antenna in a vacuum, which corresponds to a receiving antenna in a medium via reciprocity theorem (see, e.g. (Schelkunoff & Friis, 1952; Balanis, 1997)). The current at ports 1 and 2 is set to an arbitrary value of $I_a = 1A$, while currents at the opposite sides of the SC body for each dipole—ports 3 and 4, respectively—are set to $-I_a$. Middle panel shows one-dimensional cut through the AWAS solution along x axis with normalized values of the current. The normalized current j_x/I_a is found to be lower in intensity within segments 1 and 3, with a minimum value at $1-\zeta \approx 2/3$ of maximum at ports 1 and 3. Therefore, the resulting profile suggests a linear decay inside the SC body, with a minimum being different for a factor ζ compared to the one at the terminals. The numerical value $\zeta \sim 0.33$ is justified *a posteriori* in application to FIELDS data. This is notably lower than the prediction of maximum current throughout the SC body (Meyer-Vernet & Perche, 1989), given by pink dashed line. This current distribution will be used to calculate the antenna response, and then QTN spectrum.

3 Results and Discussion

3.1 Antenna response function for FIELDS

Assuming a current in the x direction, the Fourier transform of the current distribution calculated by AWAS is given as

$$j_x(k_x) = \frac{2\big(\zeta(\cos(k_x d) - 1) + k_x d \sin(k_x d)\big)}{k_x^2 d} - \frac{2(k_x L_{ant} \sin(k_x d) + \cos(k_x(d + L_{ant})) - \cos(k_x d))}{k_x^2 L_{ant}} \tag{4}$$

This expression can be directly inserted in Equation 3. While analytical integration of this expression is not possible, a numerical solution is given as a black line on the *bottom panel* of Figure 1. The obtained function has similarities with both linear and spherical dipole solutions, with the two peaks corresponding to the peaks of these two functions. Namely, for very large wavelengths (small k) the antenna samples waves that span across the entire SC. In this regime, the response is dominated by the current close to and across the SC body, having the dominant signal for the case of maximum current through the SC body (magenta), while AWAS solution has a lower response due to non-zero value of parameter ζ. For smaller wavelengths (larger k), the antenna arms increasingly sample uncorrelated signals. Here, the response of a hypothetical configuration with zero SC current (grey) starts behaving like a dipole of infinitely small spheres at distance $2L_{ant}$ (orange), while the AWAS solution shows a slight increase in signal due to this effect before settling to a linear decrease characteristic for a linear dipole with no gap (blue).

We interpret this result as a consequence of the ratio $L_{ant}/d \sim 1$. If the antenna arms are long compared to the gap ($L_{ant}/d \gg 1$), then the gap can be neglected, reducing the problem to the one encountered by multiple previous missions. Another asymptotic behavior is for the case $L_{ant}/d \ll 1$, where it reduces to a theoretical double sphere dipole configuration. However, as neither of these approximate results was valid for *PSP* configuration, numerical evaluation of ARF is necessary.

3.2 Plasma parameters from QTN spectroscopy

In this Section, we apply the new antenna response model, detailed in Section 2.3, to QTN spectra from *PSP* E7 to extract electron VDF parameters. The *left panels* of Figure 2 show examples of fits to 1-minute median values of RFS data sampled with unbiased V1-V2 dipole. Due to the very large number of sampled spectra during each of the 1-minute intervals, every panel shown represents a median of 14-17 downloaded spectra. Each spectrum downloaded from the spacecraft is an average of 40-80 on-board samples. Therefore, an instrument performs a total of 680-1360 observations per minute, and estimated uncertainty of the 1-minute averaged spectrum data points is $0.05-0.08$ dB. The fitted part of the spectrum, shown as green dots, is essentially comprised of only QTN, instrument noise and galaxy radiation contributions, which allows for an accurate determination of electron VDF parameters with very small uncertainties. For each of 64 1-minute spectra (sampled for 8 days during 8 minutes per day when no antenna biasing was applied; see Section 2.1), we use multiple sets of initial guesses for electron parameters n_e, T_c, n_h/n_c and T_h/T_c to find absolute χ^2 minimum, and also visually inspect the fits. Then, the results from these 1-minute fits are used as an initial guess for fitting the spectra in full resolution.

On *right panels*, we compare the best fit QTN model that uses the current distribution calculated in Section 2.3 with previously applied models. As already noted above, neglecting the gap between the antenna arms (blue) does not reproduce the measured spectrum neither close to f_p nor at high frequencies. Two asymptotic SC body current models also do not produce accurate representations of the observed spectrum—if maximum uniform current is assumed (magenta), the signal is notably overestimated in the vicinity of f_p, while setting the SC current to zero in the gap region both underestimates the signal around the resonance and shows a 'sphere dipole-like' behavior at high frequencies, where fluctuations of larger wavelength dominantly contribute to the spectrum (Meyer-Vernet, 1979). The different shape of the illustrated curves compared to the observed spectra makes any fitting procedure unfeasible, and we were not able to obtain satisfying overall agreement with observations, or sensible values of VDF moments with any of the previously applied current distribution models. Variation of the parameter ζ by more than $\sim 2-3\%$ also disables the model from meaningfully converging to the data, regardless of the plasma parameters used.

Figure 3 illustrates median values of fitted n_e and T_c for sets of four 1-minute unbiased intervals, plotted as black dots. We find agreement within 20% between total electron density and proton density provided by SPAN-I fits. We do not compare our results with electron density provided by SPAN-E, as it is already calibrated to f_p values obtained from the QTN plasma peak. This discrepancy is not surprising as, even though n_e is related to plasma peak frequency and is therefore the most reliable parameter in the QTN analysis, SPAN-I has a large fraction of the proton VDF moving in and out of the instrument field of view due to both instrument orientation with respect to the sunward direction (see Kasper et al. (2016); Woodham et al. (2021) for details of SPAN-I setup) and plasma flow following magnetic field reversals or 'switchbacks', which occur at timescales from seconds to tens of minutes (see e.g. Dudok de Wit et al. (2020); Martinović et al. (2021)). The brown line shows the values of the n_e obtained using the method introduced in Moncuquet et al. (2020) (further on referred to as M20). The M20 method relies on combination of plasma peak tracing based on the steepest slope in the QTN signal (Moncuquet et al., 2005; Kasaba et al., 2020) and fitting limited parts of the spectrum below f_p using the antenna response function given at Meyer-Vernet and Perche (1989) (violet lines at *middle* and *bottom* panels of Figure 1). Density values between the two data sets obtained from QTN observations are similar to the level of M20 n_e uncertainties (orange error bars), that are of the order of $\sim 9\%$ due to the instrument resolution. A small systematic discrepancy is notable, probably due to dependency of the plasma peak location in the frequency space from L_{ant}/L_D ratio; see Figure 2 in (Meyer-

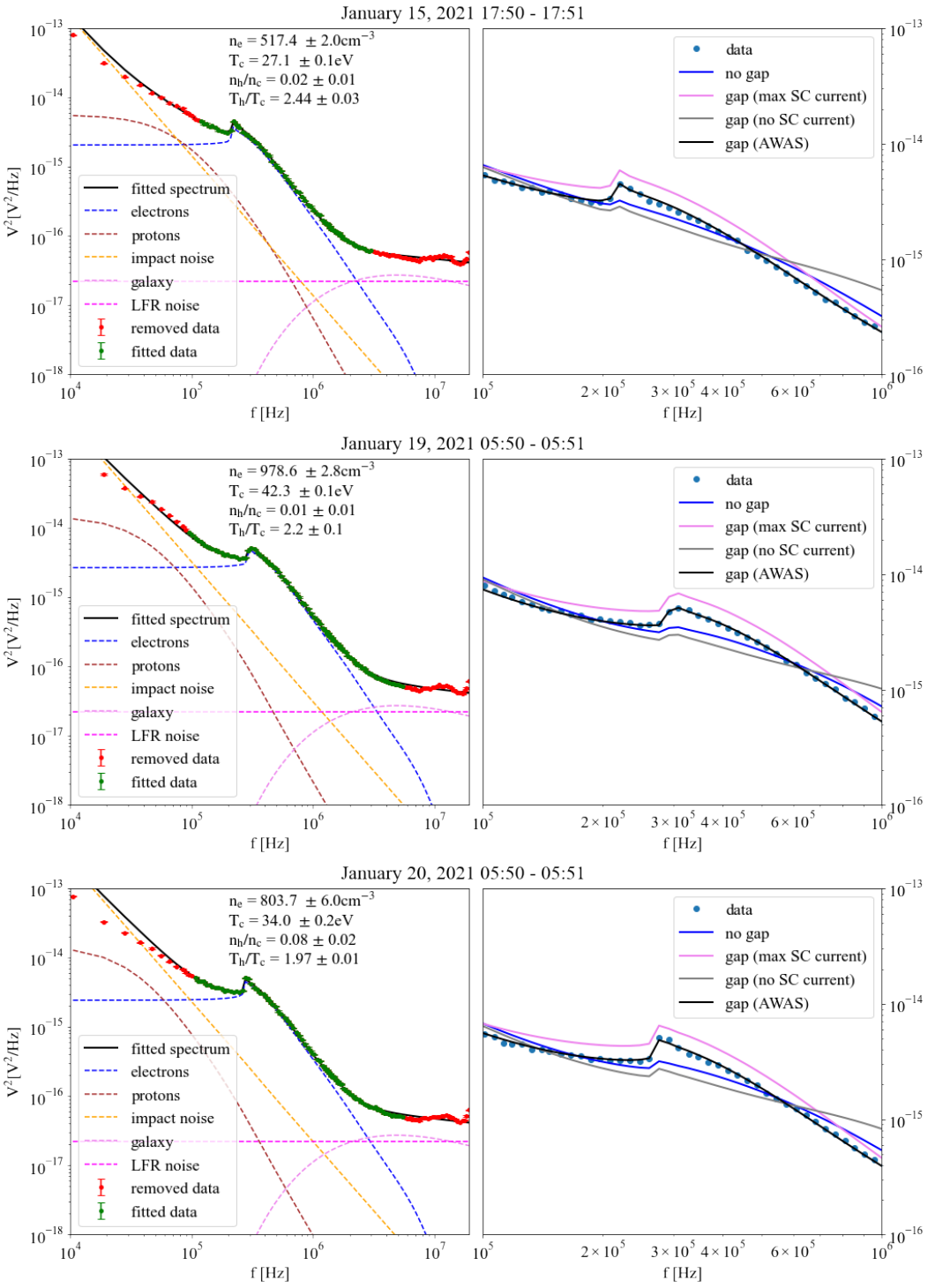

Figure 2. Three examples of the QTN spectrum fit. *Left:* Example of the QTN model fits to 1-minute median values of LFR V1-V2 dipole data with obtained electron parameter values and uncertainties, with $L_{ant}/L_D \approx [1.25, 1.37, 1.38]$ from top to bottom, respectively. *Right:* Comparison of the QTN model assuming current distribution calculated via AWAS (same parameters as on the *left panels*) with other theoretical models illustrated in Figure 1, using the same color coding. Note that the double sphere dipole spectrum is an order of magnitude above the data level and is not shown.

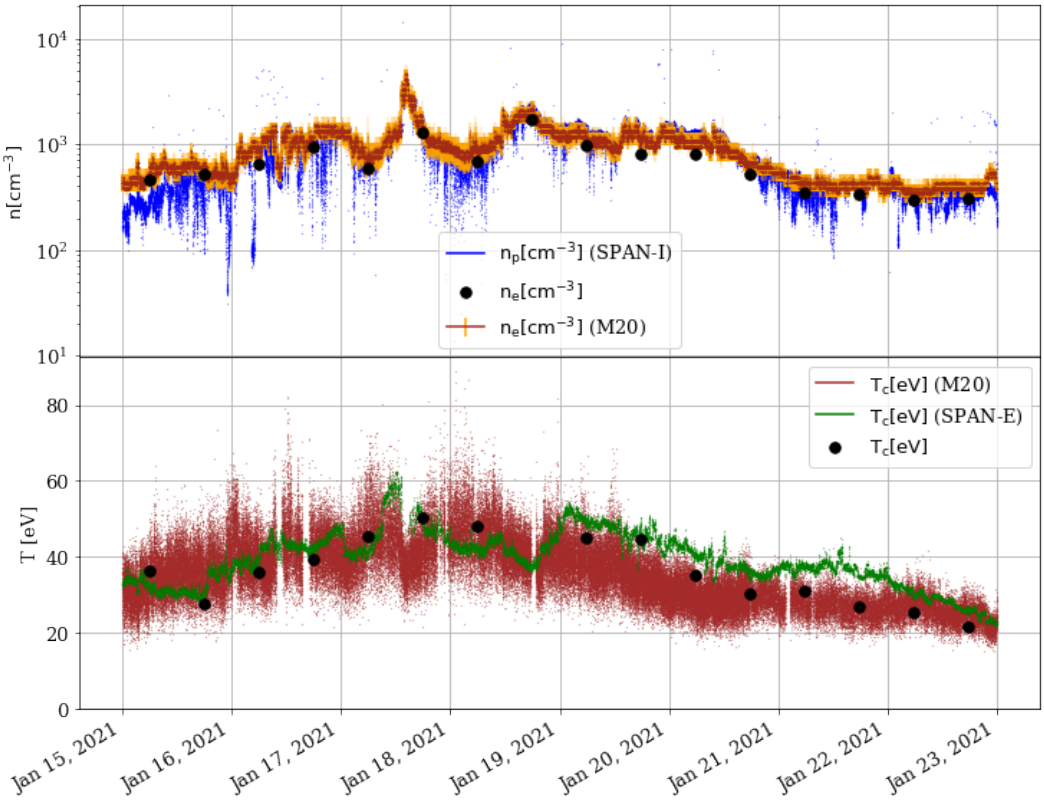

Figure 3. Overview of 1-minute median RFS observations fit, comparing proton (SPAN-I, blue) and electron densities from QTN spectroscopy using M20 algorithm (brown) and our model (black) on *top panel*; and electron core temperatures from SPAN-e (green) with both QTN data sets on *bottom panel*. Parameter uncertainties for black dots are of the order of the symbol size. The values of T_c from SPAN-E and our method do not differ for more than 10% for higher, and no more than 25% for lower temperatures. The missing interval in the afternoon of January 18 had a clearly resolved plasma peak, but also a significantly increased non-QTN signal below f_p, and confident estimation of T_c was not possible.

Vernet & Perche, 1989) for more details. These small corrections will be discussed in length in the future when a more robust data sets become available from both later Encounters and biased intervals.

Values of T_c are in overall agreement with SPAN-E results, with discrepancies within 10% closer to the *PSP* E7 closest approach, increasing to $\sim 25\%$ outbound. The difference between the two sets of results is reasonably small and we consider that its variation may be due to the change in contribution of the electron noise to the overall QTN spectrum. First, as electron temperature increases, the error in $V_{\rm pn}^2$ estimate due to the antenna orientation (Issautier et al., 1999) becomes less significant. Second, the importance of the impact noise decreases below f_p as T_c increases and the L_{ant}/L_D ratio increase. The increase in discrepancy matches with the decrease of L_{ant}/L_D from $\sim 1.4-1.5$ to ~ 1 during the last three days of the observed interval. Also, precision of the SPAN-E parameters is increased with the VDF moments due to increased signal-to-noise ratio. Our results show a very good agreement in terms of general trend with T_c values provided by M20, and fall within the range of large variations. As already noted for density, a thorough discussion on the differences between the different techniques will require future analysis of unbiased intervals and is not within the scope of this paper.

Figure 4 shows the fitted values obtained from full resolution measurements, which do not notably deviate from initial 1-minute fits. Standard deviations are less than 3% for n_e (approximately half of the instrument resolution) and less than 15% for T_c. These results demonstrate the potential for the usage of full resolution *PSP* QTN measurements to accurately extract electron VDF parameters in the near-Sun environment, as well as for advanced data products, such as level of the density fluctuations at sub-ion scales. For unbiased intervals, M20 values of T_c are not provided, while values of n_e are not shown due to very large uncertainties, which make direct comparison inconvenient.

4 Conclusions

QTN spectroscopy is a powerful in situ tool to accurately yield electron plasma parameters from levels of electric field fluctuations measured by an antenna in a plasma. The unique configuration of the PSP/FIELDS antennas caused previously applied antenna response models to either under- or overestimate the theoretical predictions around electron plasma frequency, and therefore made fitting of the full frequency range of QTN spectra unfeasible. In this article, we propose a new model of for the antenna response that using a SC current distribution calculated via simplified *PSP* geometry scheme in AWAS software. Fitting of the generic QTN model to observations provides accurate values of electron VDF parameters, with very low uncertainties and small spreads over minutes-long time intervals.

Here, we must note that a more realistic description of the suprathermal electron VDF as measured by *PSP* would include a significant strahl population, (Halekas et al., 2020). A detailed description of how strahl electrons affect QTN spectra is an open question and is a matter of future research. Therefore, even though our examples are in agreement with recently measured strahl temperatures being ~ 100 eV (Berčič et al., 2020), initial scarce calculations show that the peak width, and therefore n_h, might be primarily affected by the strahl, and the results for suprathermal parameters from this model should be handled with care.

The results shown here are intended to enable future studies, primarily by expanding this model to account for biased antenna signals, providing a full survey of VDF moments throughout multiple *PSP* encounters. In the theoretical realm, the primary remaining open question is the effect of the strahl population, which is expected to be largely increased as we approach the Sun (Maksimović, Zouganelis, et al., 2005; Štverak et al., 2009; Berčič et al., 2020), on the QTN spectrum. The effects of strahl are expected to

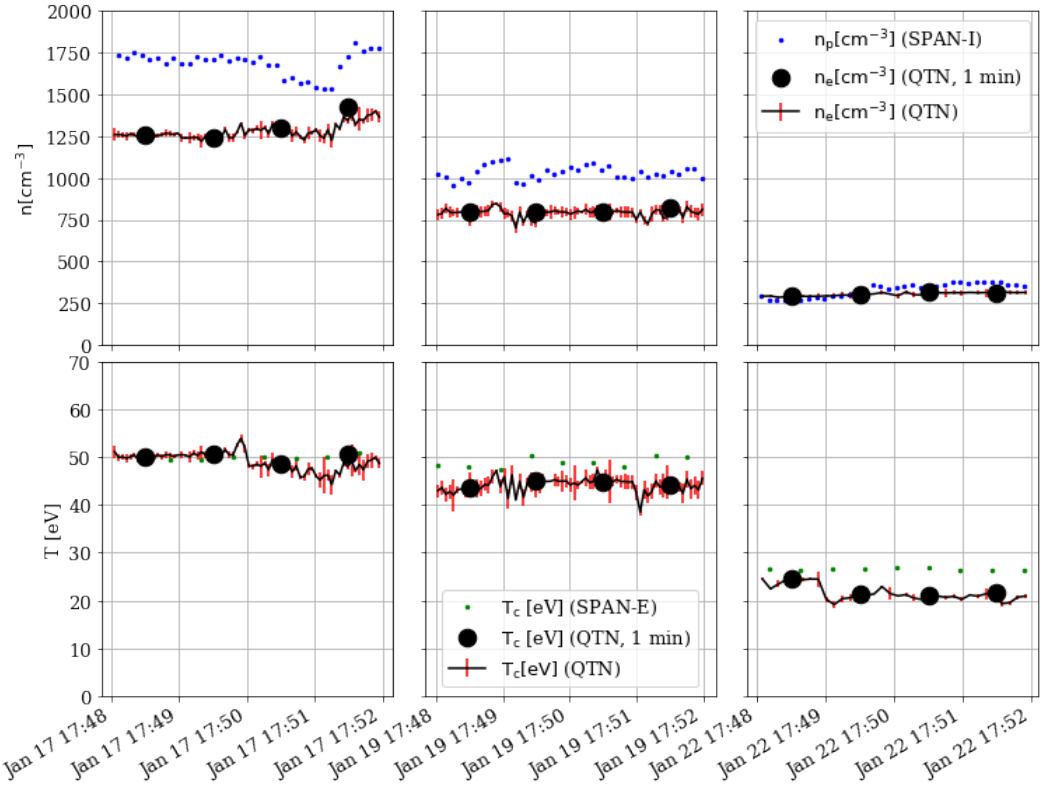

Figure 4. Comparison of SPAN parameters (same spatial and color scheme as on Figure 3) for three example intervals from E7 not represented on Figure 2. The full resolution fits are shown with error bars. The spread of T_c values obtained by QTN spectroscopy is lower than 20% for all 1-minute intervals.

be important around f_p. As mentioned above, visibility of the plasma peak, and therefore the strahl signal, depends on the L_{ant}/L_D ratio, which is steadily increasing as we approach the Sun (Maksimović, Issautier, et al., 2005) and has surpassed unity during the closest approach of *PSP* in E7. As future encounters in 2023 and 2024 are expected to make *PSP* the first non-spinning SC with $L_{ant}/L_D \gg 1$, there is a potential for plasma resonance peak to be sufficiently well resolved for small differences between halo and strahl signals to be tested by observations.

Acronyms

PSP Parker Solar Probe
QTN Quasi-Thermal Noise
VDF Velocity Distribution Function
STEREO Solar TErrestial REsearch Observatory
AWAS Analysis of Wire Antennas and Scatterers
SWEAP Solar Wind Electrons, Protons & Alphas
SPAN-I(E) Solar Probe ANalyzer for Ions (Electrons)
RFS Radio Frequency Spectrometer
LFR Low Frequency Receiver
HFR High Frequency Receiver
SPDF Space Physics Data Facility

Acknowledgments

We thank Michel Moncuquet for enlightening discussions on the LFR data processing. Parker Solar Probe was designed, built, and is now operated by the Johns Hopkins Applied Physics Laboratory as part of NASA's Living with a Star (LWS) program (contract NNN06AA01C). Support from the LWS management and technical team has played a critical role in the success of the Parker Solar Probe mission. The authors acknowledge CNES (Centre National d Etudes Spatiales), CNRS (Centre National de la Recherche Scientifique), the Observatoire de PARIS, NASA and the FIELDS/RFS team for their support to the PSP/SQTN data production, and the CDPP (Centre de Donnees de la Physique des Plasmas) for their archiving and provision. The FIELDS experiment was developed and is operated under NASA contract NNN06AA01C. The SWEAP Investigation and this publication are supported by the PSP mission under NASA contract NNN06AA01C. M. M. Martinović and K. G. Klein were financially supported by NASA grant 80NSSC19K0521. PSP FIELDS LFR/HFR data is avaialble at `http://sprg.ssl.berkeley.edu/data/psp/data/sci/fields/l2/rfs_lfr/` and `http://sprg.ssl.berkeley.edu/data/psp/data/sci/fields/l2/rfs_hfr/`. PSP SWEAP SPAN-I/SPAN-E data can be found at `http://sweap.cfa.harvard.edu/pub/data/sci/sweap/spi/L3/` and `http://sweap.cfa.harvard.edu/pub/data/sci/sweap/spe/L3/`. The M20 data set is accessible at French national data centre for natural plasmas of the solar system `http://www.cdpp.eu/` under `Missions@Archive / PARKER SOLAR PROBE MISSION / PARKER SOLAR PROBE FIELDS Experiment / PARKER SOLAR PROBE FIELDS - Simplified Quasi-Thermal Noise (SQTN) Spectroscopy`.

References

Andronov, A. A. (1966). Импеданс и шумы антенны (зонда) в космической плазмы. *Космические исследования*, *4*, 558–567.

Balanis, C. A. (1997). *Antenna theory and analysis and design*. New York, USA: Wiley.

Bale, S. D., Badman, S. T., Bonnell, J. W., Bowen, T. A., Burgess, D., Case, A. W.,

... Wygant, J. R. (2019, December). Highly structured slow solar wind emerging from an equatorial coronal hole. *Nature*, *576*(7786), 237-242. doi: 10.1038/s41586-019-1818-7

Bale, S. D., Goetz, K., Harvey, P. R., Turin, P., Bonnell, J. W., Dudok de Wit, T., ... Wygant, J. R. (2016, December). The FIELDS Instrument Suite for Solar Probe Plus. Measuring the Coronal Plasma and Magnetic Field, Plasma Waves and Turbulence, and Radio Signatures of Solar Transients. *Space Science Reviews*, *204*(1-4), 49-82. doi: 10.1007/s11214-016-0244-5

Berčič, L., Larson, D., Whittlesey, P., Maksimović, M., Badman, S. T., Landi, S., ... Stevens, M. L. (2020, April). Coronal Electron Temperature Inferred from the Strahl Electrons in the Inner Heliosphere: Parker Solar Probe and Helios Observations. *The Astrophysical Journal*, *892*(2), 88. doi: 10.3847/1538-4357/ab7b7a

Bonnell, J. W., Mozer, F., Bale, S. D., Case, A. W., Goodrich, K., Harvey, P., ... Wygant, J. R. (2019, December). In-Flight DC and Low-Frequency Electric Field Calibration for the Parker Solar Probe. In *Agu fall meeting abstracts* (Vol. 2019, p. SH13C-3439).

Chateau, Y. F., & Meyer-Vernet, N. (1989). Electrostatic noise in non-maxwellian plasmas: Flat-top distribution function. *Journal of Geophysical Research*, *94*, 15407–15414.

Đorđević, A. R., Bažd ar, M. B., Petrović, V. V., Olcan, D. I., Sarkar, T. K., & Harrington, R. F. (2002). *Awas for windows version 2.0: Analysis of wire antennas and scatterers (software and user's manual).* 685 Canton St, Norwood, MA 02062, USA: Artech House.

Đorđević, A. R., Bažd ar, M. B., Sarkar, T. K., & Harrington, R. F. (1991). Solution of two-potential equation for wire structures using polynomial expansion and pulse testing functions. In *1991 seventh international conference on antennas and propagation, icap 91 (iee)* (pp. 540–543).

Đorđević, A. R., Popović, B. D., & Dragović, M. B. (1979). A method for rapid analysis of wire-antenna structures. *Archiv für Elektrotechnik*, *61*(1), 17–23.

Dudok de Wit, T., Krasnoselskikh, V. V., Bale, S. D., Bonnell, J. W., Bowen, T. A., Chen, C. H. K., ... Whittlesey, P. L. (2020, February). Switchbacks in the Near-Sun Magnetic Field: Long Memory and Impact on the Turbulence Cascade. *The Astrophysical Journal Supplement Series*, *246*(2), 39. doi: 10.3847/1538-4365/ab5853

Fejer, J. A., & Kan, J. R. (1969). Noise spectrum received by an antenna in a plasma. *Radio Science*, *4*, 721–728.

Halekas, J. S., Whittlesey, P., Larson, D. E., McGinnis, D., Maksimovic, M., Berthomier, M., ... Harvey, P. R. (2020, February). Electrons in the Young Solar Wind: First Results from the Parker Solar Probe. *The Astrophysical Journal Supplement Series*, *246*(2), 22. doi: 10.3847/1538-4365/ab4cec

Harrington, R. F. (1993). *Field computation by moment methods.* Wiley-IEEE Press.

Hoang, S., Steinberg, J. L., Epstein, G., Tilloles, P., Fainberg, J., & Stone, R. G. (1980). The low-frequency continuum as observed in the solar wind from isee 3 - thermal electrostatic noise. *Journal of Geophysical Research*, *85*, 3419–3430.

Issautier, K., Meyer-Vernet, N., Moncuquet, M., & Hoang, S. (1996). A novel method to measure the solar wind speed. *Geophysical Research Letters*, *23*, 1649–1652.

Issautier, K., Meyer-Vernet, N., Moncuquet, M., & Hoang, S. (1999). Quasi-thermal noise in a drifting plasma: Theory and application to solar wind diagnostic on ulysses. *Journal of Geophysical Research*, *104*, 6691–6704.

Issautier, K., Perche, C., Hoang, S., Maksimović, M., Lacombe, C., Bougeret, J.-L. H., & Salem, C. (2005). Solar wind electron density and temperature over solar cycle 23: Thermal noise measurements on wind. *Advances in Space*

Research, *35*, 2141–2146.

Kasaba, Y., Kojima, H., Moncuquet, M., Wahlund, J.-E., Yagitani, S., Sahraoui, F., ... Usui, H. (2020, June). Plasma Wave Investigation (PWI) Aboard BepiColombo Mio on the Trip to the First Measurement of Electric Fields, Electromagnetic Waves, and Radio Waves Around Mercury. *"Space Science Reviews"*, *216*(4), 65. doi: 10.1007/s11214-020-00692-9

Kasper, J. C., Abiad, R., Austin, G., Balat-Pichelin, M., Bale, S. D., Belcher, J. W., ... Zank, G. (2016, December). Solar Wind Electrons Alphas and Protons (SWEAP) Investigation: Design of the Solar Wind and Coronal Plasma Instrument Suite for Solar Probe Plus. *Space Science Reviews*, *204*(1-4), 131-186. doi: 10.1007/s11214-015-0206-3

Kellogg, P. (1981). Calculation and observation of thermal electrostatic noise in solar wind plasma. *Plasma Physics*, *23*, 735–751.

Kuehl, H. H. (1966). Resistance of a short antenna in a warm plasma. *Radio Science*, *1*, 971–976.

Kuehl, H. H. (1967). Computations of the resistance of a short antenna in a warm plasma. *Radio Science*, *2*, 73–76.

Le Chat, G., Issautier, K., Meyer-Vernet, N., & Hoang, S. (2011). Large-scale variation of solar wind electron properties from quasi-thermal noise spectroscopy: Ulysses measurements. *Solar Physics*, *271*, 141–148.

Liu, M., Issautier, K., Meyer-Vernet, N., Moncuquet, M., Maksimovic, M., Halekas, J. S., ... Stevens, M. L. (2021, June). Solar wind energy flux observations in the inner heliosphere: first results from Parker Solar Probe. *Astronomy & Astrophysics*, *650*, A14. doi: 10.1051/0004-6361/202039615

Maksimović, M., Bale, S. D., Berčič, L., Bonnell, J. W., Case, A. W., Wit, T. D. d., ... Whittlesey, P. L. (2020, February). Anticorrelation between the Bulk Speed and the Electron Temperature in the Pristine Solar Wind: First Results from the Parker Solar Probe and Comparison with Helios. *The Astrophysical Journal Supplement Series*, *246*(2), 62. doi: 10.3847/1538-4365/ab61fc

Maksimović, M., Bale, S. D., Chust, T., Khotyaintsev, Y., Krasnoselskikh, V., Kretzschmar, M., ... Zouganelis, I. (2020, October). The Solar Orbiter Radio and Plasma Waves (RPW) instrument. *Astronomy & Astrophysics*, *642*, A12. doi: 10.1051/0004-6361/201936214

Maksimovic, M., Bougeret, J. L., Perche, C., Steinberg, J. T., Lazarus, A. J., Viñas, A. F., & Fitzenreiter, R. J. (1998). Solar wind density intercomparisons on the wind spacecraft using waves and swe experiments. *Geophysical Research Letters*, *25*, 1265–1268.

Maksimovic, M., Hoang, S., Meyer-Vernet, N., Moncuquet, M., Bougeret, J. L., Phillips, J. L., & Canu, P. (1995, Oct). Solar wind electron parameters from quasi-thermal noise spectroscopy and comparison with other measurements on Ulysses. *Journal of Geophysical Research*, *100*(A10), 19881-19892. doi: 10.1029/95JA01550

Maksimović, M., Issautier, K., Meyer-Vernet, N., Perche, C., Moncuquet, M., Zouganelis, Y., ... Bougeret, J. L. (2005). Solar wind electron temperature and density measurements on the solar orbiter with thermal noise spectroscopy. *Advances in Space Research*, *35*, 1471–1473.

Maksimović, M., Zouganelis, Y., Chaufray, J. Y., Issautier, K., Scime, E. E., Littleton, J. E., ... Elliot, H. (2005). Radial evolution of the electron distribution functions in the fast solar wind between 0.3 and 1.5 au. *Journal of Geophysical Research*, *110*, A09104.

Martinović, M. M. (2016). *A study of quasi-thermal noise and shot noise in space plasmas* (Unpublished doctoral dissertation). LESIA, Observatoire de Paris / University of Belgrade.

Martinović, M. M., Klein, K. G., Gramze, S. R., Jain, H., Maksimović, M., Zaslavsky, A., ... Simić, Z. (2020, August). Solar Wind Electron Parame-

ters Determination on Wind Spacecraft Using Quasi-Thermal Noise Spectroscopy. *Journal of Geophysical Research (Space Physics)*, *125*(8), e28113. doi: 10.1029/2020JA028113

Martinović, M. M., Klein, K. G., Huang, J., Chandran, B. D. G., Kasper, J. C., Lichko, E., ... Bale, S. D. (2021, May). Multiscale Solar Wind Turbulence Properties inside and near Switchbacks Measured by the Parker Solar Probe. *The Astrophysical Journal*, *912*(1), 28. doi: 10.3847/1538-4357/abebe5

Martinović, M. M., Zaslavsky, A., Maksimović, M., Meyer-Vernet, N., Šegan, S., Zouganelis, Y., ... Bale, S. D. (2016). Quasi-thermal noise measurements on stereo: Kinetic temperature deduction using electron shot noise model. *Journal of Geophysical Research: Space Physics*, *121*, 129–139.

Meyer-Vernet, N. (1979). On natural noises detected by antennas in plasmas. *Journal of Geophysical Research*, *94*, 2405–2415.

Meyer-Vernet, N., Issautier, K., & Moncuquet, M. (2017). Quasi-thermal noise spectroscopy: The art and the practice. *Journal of Geophysical Research: Space Physics*, *122*, 7925–7945.

Meyer-Vernet, N., & Perche, C. (1989). Tool kit for antennae and thermal noise near the plasma frequency. *Journal of Geophysical Research*, *94*, 2405–2415.

Moncuquet, M., Lecacheux, A., Meyer-Vernet, N., Cecconi, B., & Kurth, W. S. (2005). Quasi thermal noise spectroscopy in the inner magnetosphere of saturn with cassini/rpws: Electron temperatures and density. *Geophysical Research Letters*, *32*, L20S02.

Moncuquet, M., Meyer-Vernet, N., Issautier, K., Pulupa, M., Bonnell, J. W., Bale, S. D., ... Malaspina, D. M. (2020, Feb). First In Situ Measurements of Electron Density and Temperature from Quasi-thermal Noise Spectroscopy with Parker Solar Probe/FIELDS. *The Astrophysical Journal Supplement Series*, *246*(2), 44. doi: 10.3847/1538-4365/ab5a84

Moncuquet, M., Meyer-Vernet, N., & Hoang, S. (1997). Detection of bernstein wave forbidden bands in the jovian magnetosphere: A new way to measure the electron density. *Journal of Geophysical Research*, *102*, 21697–21708.

Novaco, J. C., & Brown, L. W. (1978, Apr). Nonthermal galactic emission below 10 megahertz. *The Astrophysical Journal*, *221*, 114-123. doi: 10.1086/156009

Popović, B. D., Dragović, M. B., & Đorđević, A. R. (1982). *Analysis and synthesis of wire antennas.* Chichester, UK: John Wiley & Sons.

Pulupa, M., Bale, S. D., Bonnell, J. W., Bowen, T. A., Carruth, N., Goetz, K., ... Sundkvist, D. (2017, March). The Solar Probe Plus Radio Frequency Spectrometer: Measurement requirements, analog design, and digital signal processing. *Journal of Geophysical Research (Space Physics)*, *122*(3), 2836-2854. doi: 10.1002/2016JA023345

Schelkunoff, S. A., & Friis, H. T. (1952). *Antennas: theory and practice.* 111 River Street, Hoboken, New York 07030, USA: Wiley.

Verniero, J. L., Larson, D. E., Livi, R., Rahmati, A., McManus, M. D., Pyakurel, P. S., ... de Wit, T. D. (2020, May). Parker Solar Probe Observations of Proton Beams Simultaneous with Ion-scale Waves. *The Astrophysical Journal Supplement Series*, *248*(1), 5. doi: 10.3847/1538-4365/ab86af

Whittlesey, P. L., Larson, D. E., Kasper, J. C., Halekas, J., Abatcha, M., Abiad, R., ... Verniero, J. L. (2020, February). The Solar Probe ANalyzers—Electrons on the Parker Solar Probe. *The Astrophysical Journal Supplement Series*, *246*(2), 74. doi: 10.3847/1538-4365/ab7370

Woodham, L. D., Horbury, T. S., Matteini, L., Woolley, T., Laker, R., Bale, S. D., ... Pulupa, M. P. (2021, June). Enhanced proton parallel temperature inside patches of switchbacks in the inner heliosphere. *Astronomy and Astrophysics*, *650*, L1. doi: 10.1051/0004-6361/202039415

Zouganelis, Y., Maksimović, M., Meyer-Vernet, N., Bale, S. D., Eastwood, J. P., Zaslavsky, A., ... Kaiser, M. L. (2010). Measurements of stray antenna

capacitance in the stereo/waves instrument: Comparison of the measured voltage spectrum with an antenna electron shot noise model. *Radio science*, *45*, 1005–1009.

Štverak, S., Maksimović, M., Travniček, P., Marsch, E., Fazakerley, A. N., & Scime, E. E. (2009). Radial evolution of nonthermal electron populations in the low-latitude solar wind: Helios, cluster, and ulysses observations. *Journal of Geophysical Research*, *114*, A05104.

Figure 1.

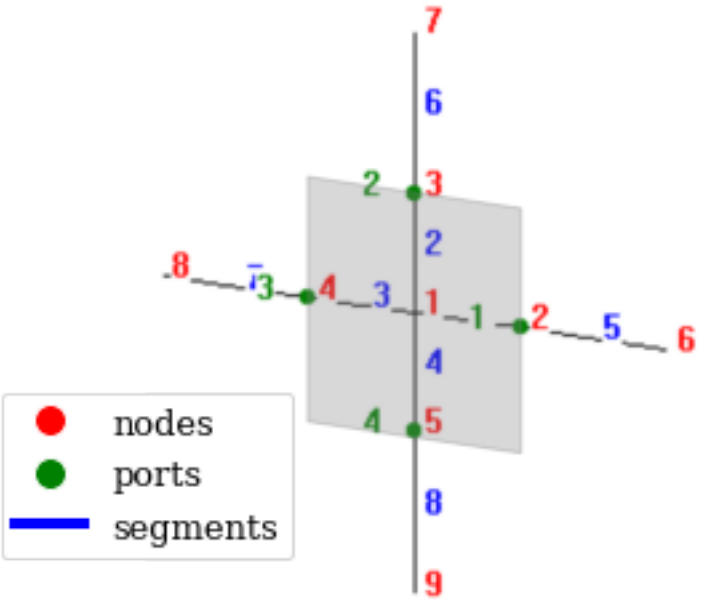
nodes
ports
segments

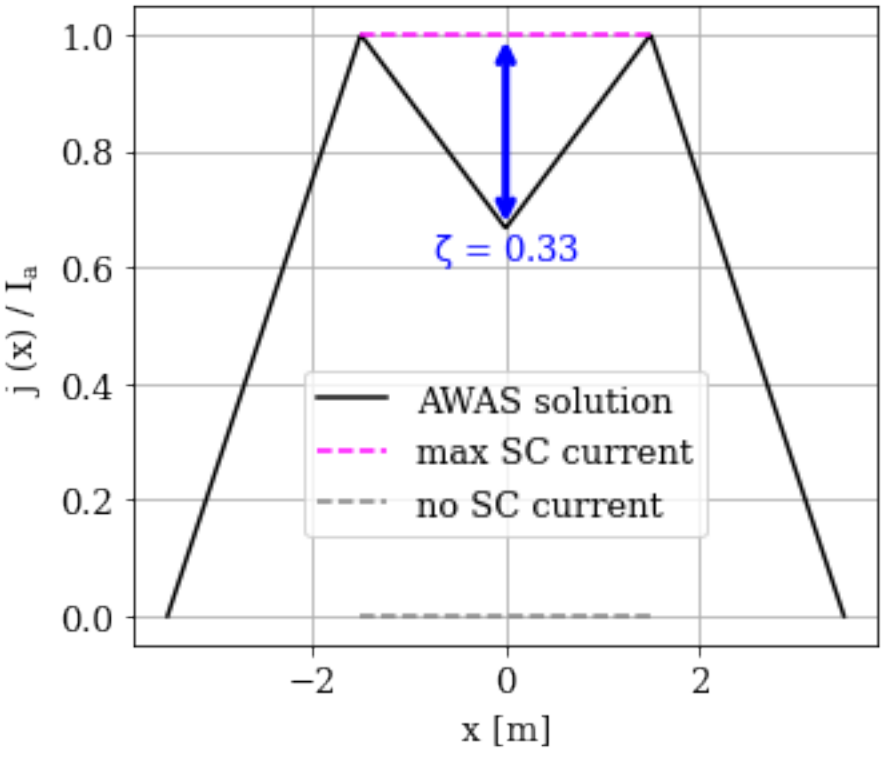
ζ = 0.33
AWAS solution
max SC current
no SC current
j (x) / I_a
x [m]

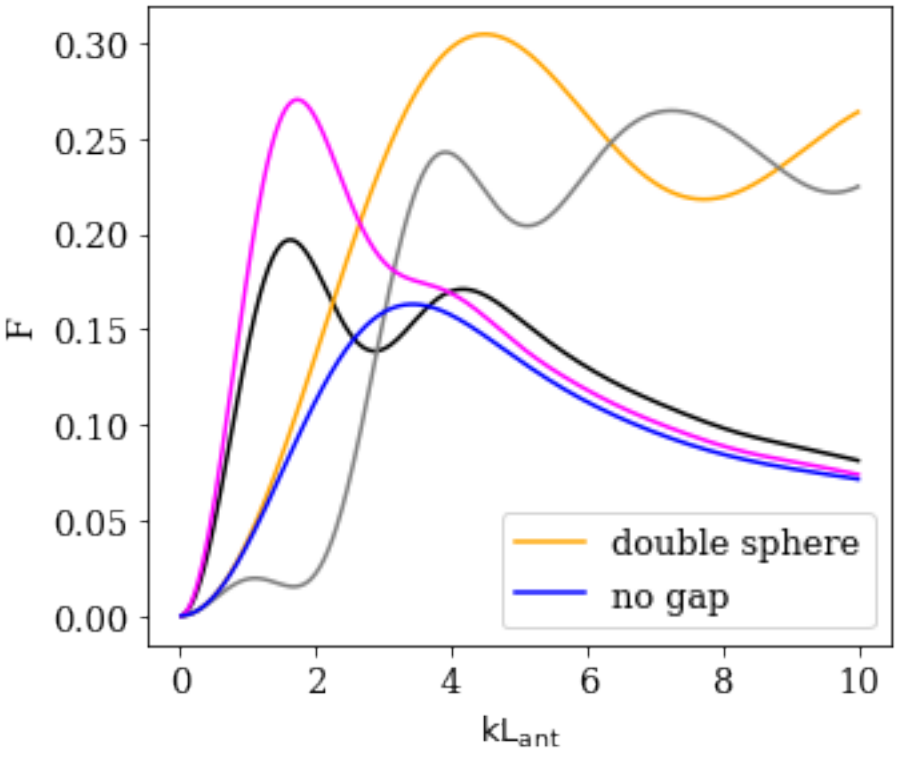
double sphere
no gap
F
kL_ant

Figure 2_1.

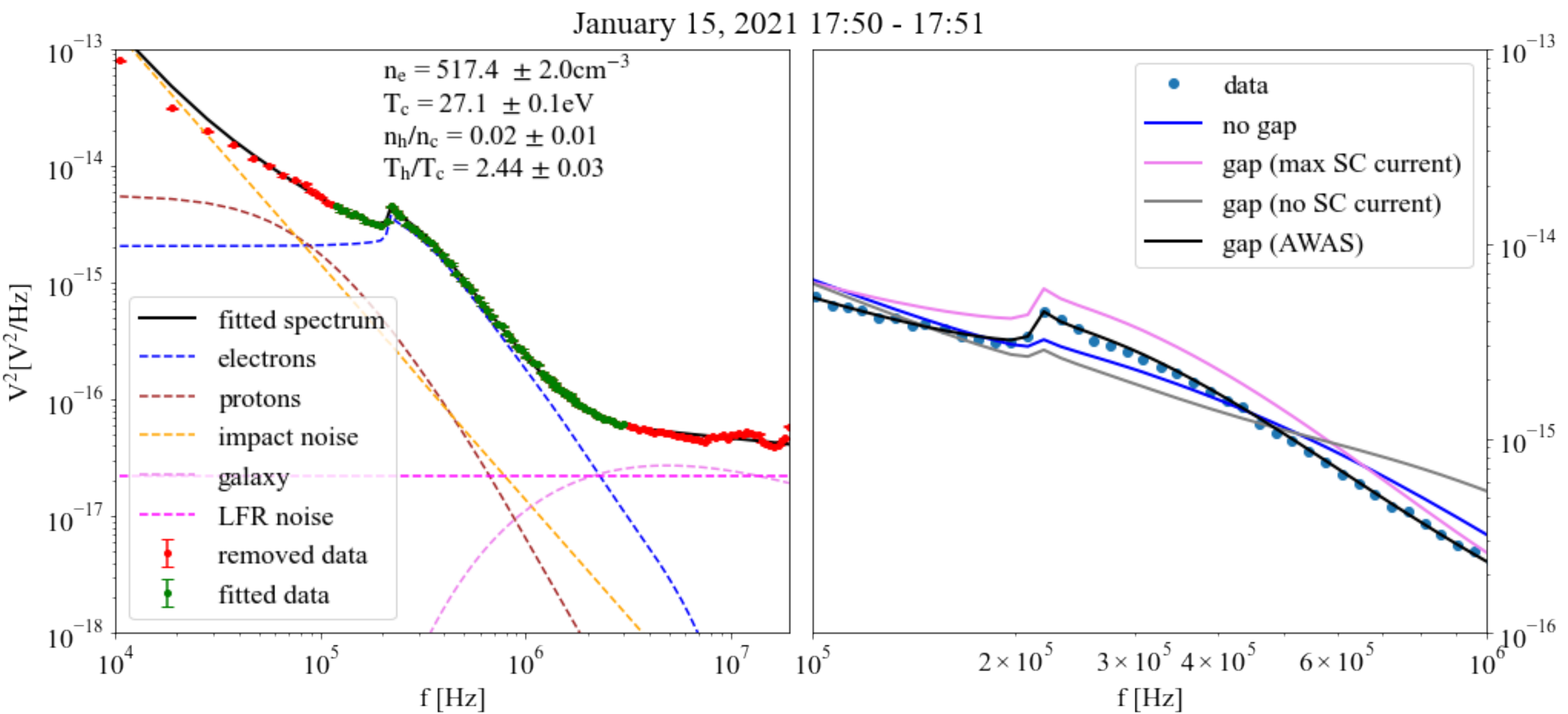
January 15, 2021 17:50 - 17:51
$n_e = 517.4 \pm 2.0 cm^{-3}$
$T_c = 27.1 \pm 0.1 eV$
$n_h/n_c = 0.02 \pm 0.01$
$T_h/T_c = 2.44 \pm 0.03$
fitted spectrum
electrons
protons
impact noise
galaxy
LFR noise
removed data
fitted data
$V^2[V^2/Hz]$
f [Hz]
data
no gap
gap (max SC current)
gap (no SC current)
gap (AWAS)
f [Hz]

Figure 2_2.

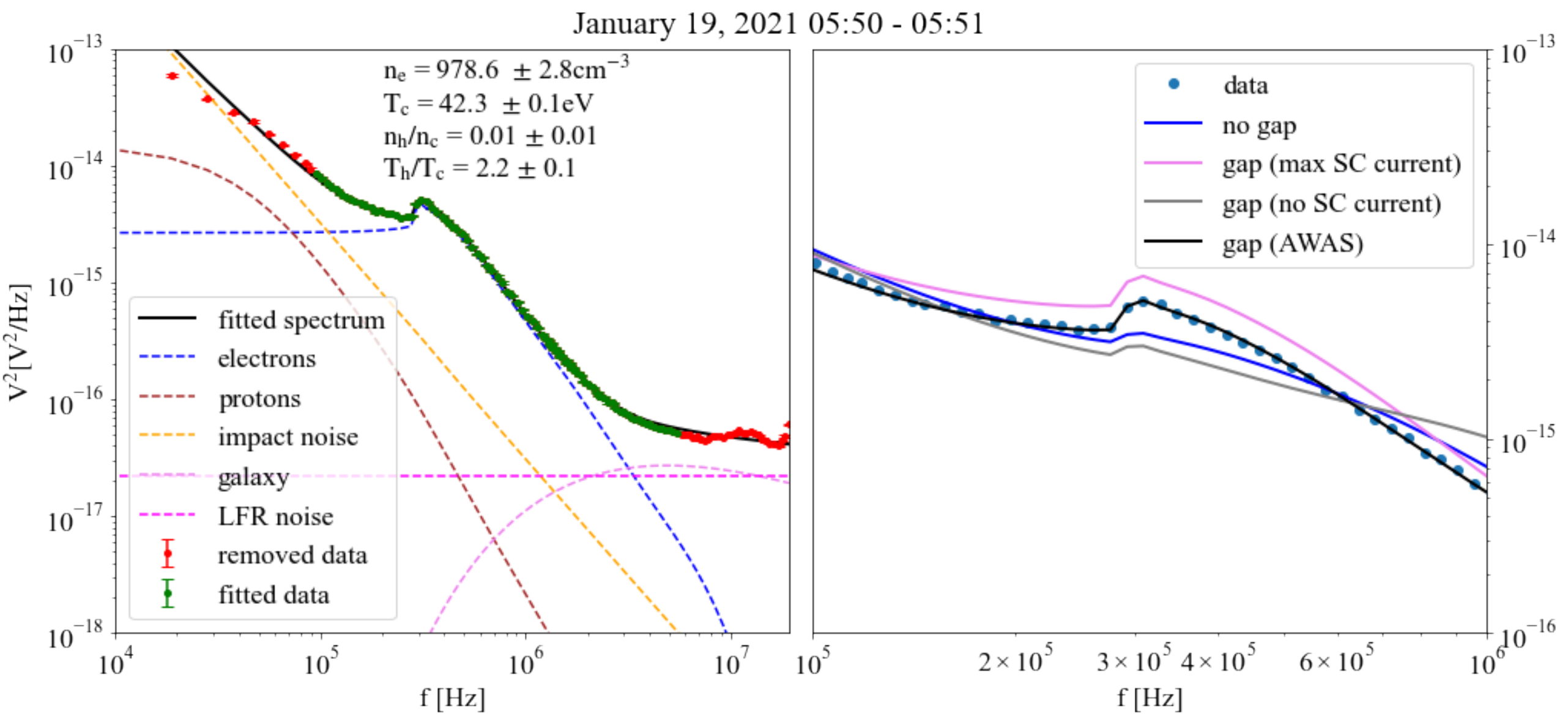
January 19, 2021 05:50 - 05:51
$n_e = 978.6 \pm 2.8 cm^{-3}$
$T_c = 42.3 \pm 0.1 eV$
$n_h/n_c = 0.01 \pm 0.01$
$T_h/T_c = 2.2 \pm 0.1$
fitted spectrum
electrons
protons
impact noise
galaxy
LFR noise
removed data
fitted data
$V^2 [V^2/Hz]$
f [Hz]
data
no gap
gap (max SC current)
gap (no SC current)
gap (AWAS)
f [Hz]

Figure 2_3.

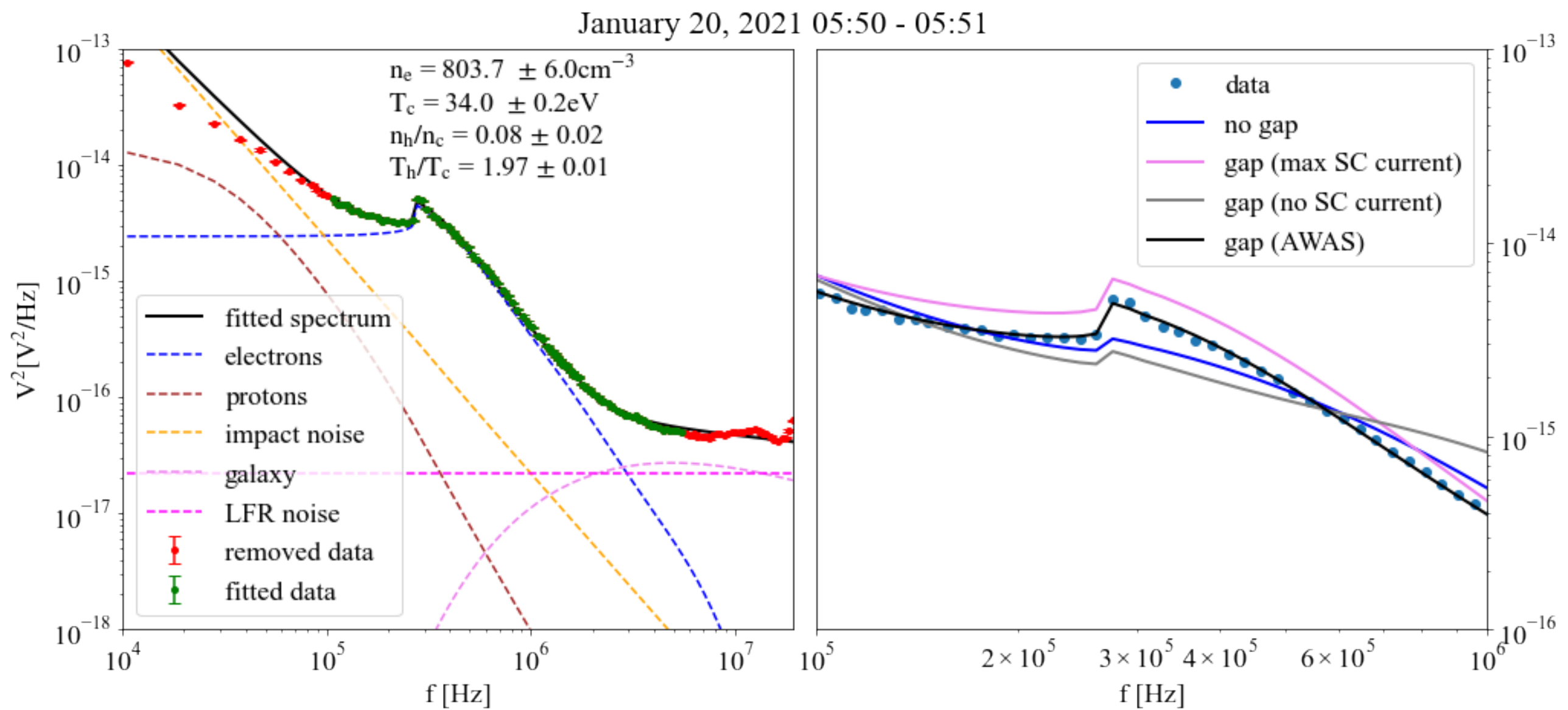
January 20, 2021 05:50 - 05:51
$n_e = 803.7 \pm 6.0 cm^{-3}$
$T_c = 34.0 \pm 0.2 eV$
$n_h/n_c = 0.08 \pm 0.02$
$T_h/T_c = 1.97 \pm 0.01$
fitted spectrum
electrons
protons
impact noise
galaxy
LFR noise
removed data
fitted data
$V^2 [V^2/Hz]$
f [Hz]
data
no gap
gap (max SC current)
gap (no SC current)
gap (AWAS)
f [Hz]

Figure 3.

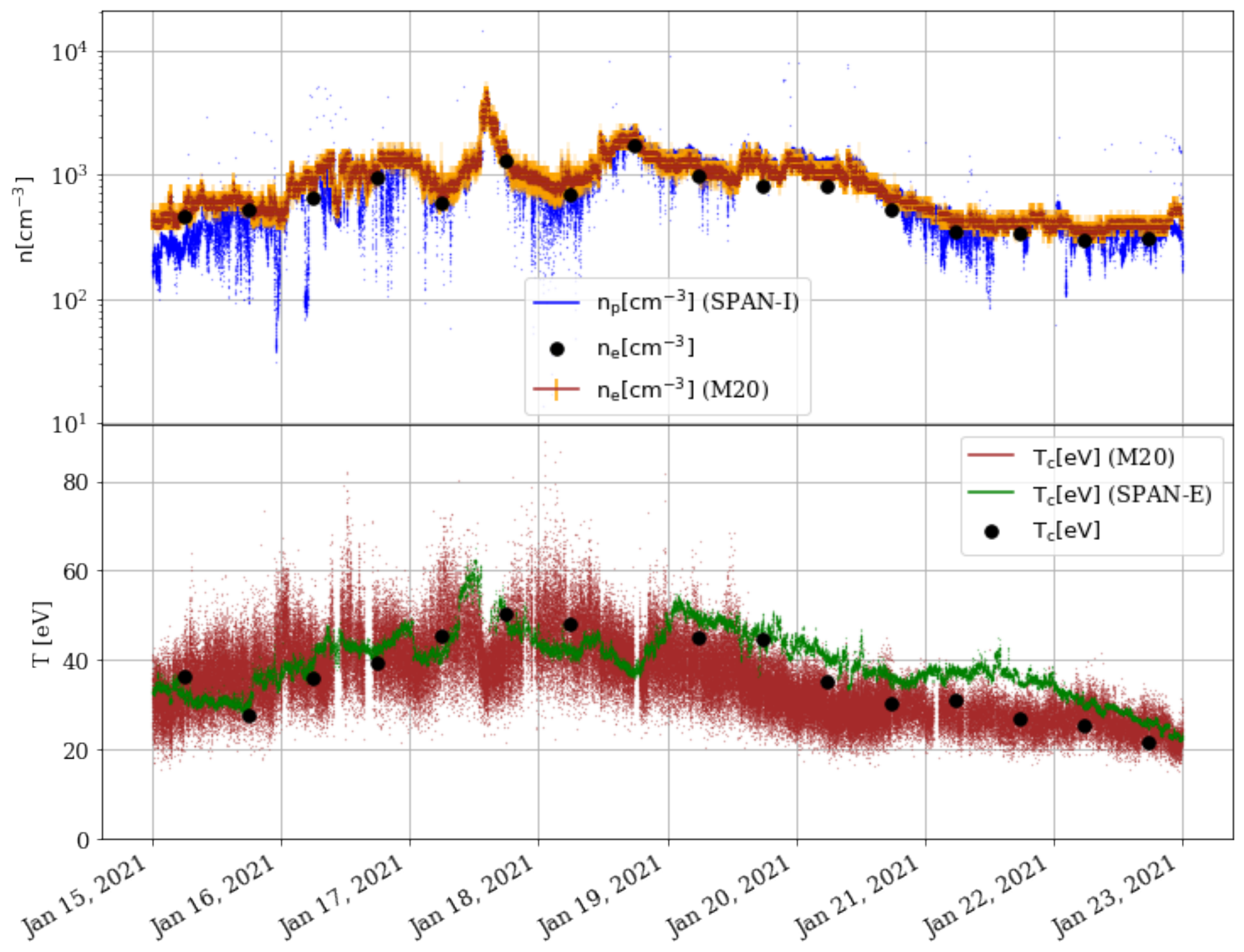
n[cm^{-3}]
10^4
10^3
10^2
10^1
n_p[cm^{-3}] (SPAN-I)
n_e[cm^{-3}]
n_e[cm^{-3}] (M20)
T [eV]
80
60
40
20
0
T_c[eV] (M20)
T_c[eV] (SPAN-E)
T_c[eV]
Jan 15, 2021
Jan 16, 2021
Jan 17, 2021
Jan 18, 2021
Jan 19, 2021
Jan 20, 2021
Jan 21, 2021
Jan 22, 2021
Jan 23, 2021

Figure 4.

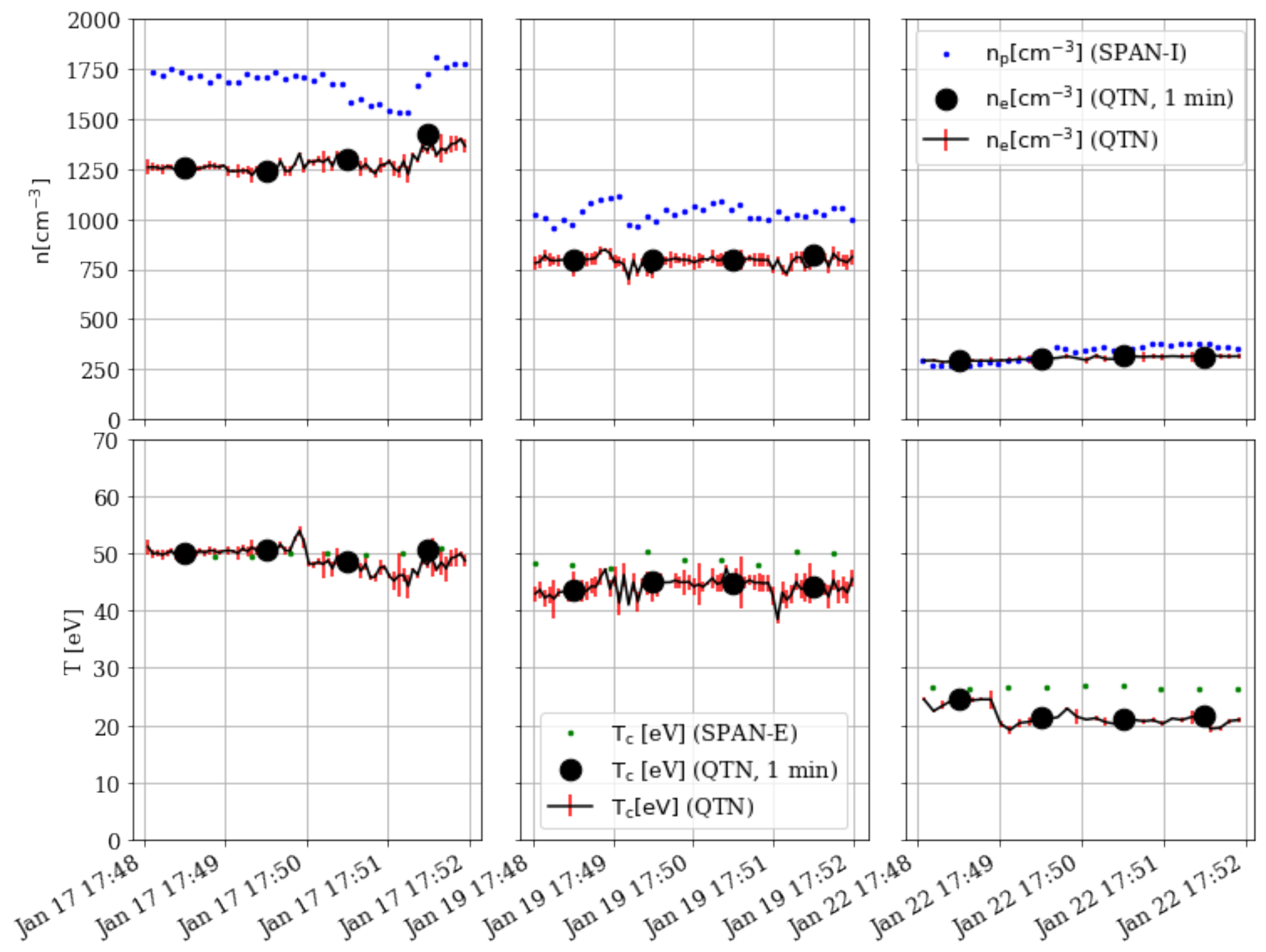
n[cm^{-3}]
T [eV]
n_p[cm^{-3}] (SPAN-I)
n_e[cm^{-3}] (QTN, 1 min)
n_e[cm^{-3}] (QTN)
T_c [eV] (SPAN-E)
T_c [eV] (QTN, 1 min)
T_c[eV] (QTN)
Jan 17 17:48
Jan 17 17:49
Jan 17 17:50
Jan 17 17:51
Jan 17 17:52
Jan 19 17:48
Jan 19 17:49
Jan 19 17:50
Jan 19 17:51
Jan 19 17:52
Jan 22 17:48
Jan 22 17:49
Jan 22 17:50
Jan 22 17:51
Jan 22 17:52